Interaction of Domain Walls with Grain Boundaries in Uniaxial Insulating Antiferromagnets

Oleksandr V. Pylypovskyi[1,2,*] Natascha Hedrich,[3] Artem V. Tomilo[1] Tobias Kosub,[1]
Kai Wagner,[3] René Hübner[1] Brendan Shields,[3] Denis D. Sheka[4] Jürgen Fassbender,[1]
Patrick Maletinsky[3] and Denys Makarov[1,†]

[1]*Helmholtz-Zentrum Dresden-Rossendorf e.V., Institute of Ion Beam Physics and Materials Research, Dresden 01328, Germany*

[2]*Kyiv Academic University, Kyiv 03142, Ukraine*

[3]*Department of Physics, University of Basel, Klingelbergstrasse 82, Basel CH-4056, Switzerland*

[4]*Taras Shevchenko National University of Kyiv, Kyiv 01601, Ukraine*

A search for high-speed and low-energy memory devices puts antiferromagnetic thin films at the forefront of spintronic research. Here, we develop a material model of a granular antiferromagnetic thin film with uniaxial anisotropy and provide fundamental insight into the interaction of antiferromagnetic domain walls with grain boundaries. This model is validated on thin films of the antiferromagnetic insulator Cr_2O_3, revealing complex mazelike domain patterns hosting localized nanoscale domains down to 50 nm. We show that the intergrain magnetic parameters can be estimated based on an analysis of high-resolution images of antiferromagnetic domain patterns examining the domain patterns' self-similarity and the statistical distribution of domain sizes. Having a predictive material model and understanding of the pinning of domain walls on grain boundaries, we put forth design rules to realize granular antiferromagnetic recording media.

I. INTRODUCTION

In the last years, there has been an intense search for ultrafast and energy-efficient memory devices [1–4]. Many promising concepts are based on materials with complex antiferromagnetic (AFM) ordering. A necessary prerequisite behind the development of AFM memory is the understanding of the underlying physics of the material: origin of chiral interactions [5], spin-orbit [6,7], and spin-transfer torques [8], topological features in momentum and real space [9,10], finite-size effects [11,12], strain effects [13–15], interaction of topologically nontrivial magnetic textures with single lattice defects [16,17], and dynamics in granular thin films [18]. Current demonstrations rely on electrically conducting AFMs as Cu-Mn-As [19,20] or Mn_2Au [21], or insulators as multiferroic $BiFeO_3$ [22–24] or magnetoelectric Cr_2O_3 [14,25–27]. Available proposals of AFM devices already include magnetoelectric spin-orbit (MESO) logic [23], AFM RAM [19], magnetoelectric RAM [25,26], and domain-wall-based memory [27]. In the family of insulating AFMs, magnetoelectric Cr_2O_3 attracts attention due to the possibility to manipulate the magnetic order parameter using magnetoelectric fields and even electric fields only [14]. Insulating thin films of Cr_2O_3 are technologically relevant, but they possess typically granular morphology [28–31]. This leads to the drastic modification of the AFM domain pattern. AFM domains are thermodynamically *unstable* in uniaxial AFMs [32,33], which is also valid for single crystals of Cr_2O_3 [27]. Therefore, a complex domain pattern observed experimentally for polycrystalline bulk Cr_2O_3 samples [34] and thin films of Cr_2O_3 (see also Refs. [28,30,31]) is expected to be induced by pinning of domain walls on grain boundaries. Peculiar features of the AFM domain landscape in thin films of Cr_2O_3 include sharp bends of domain walls and the presence of domains with sizes comparable with the grain size. Considering that the grain size can be tailored by growth parameters, granular AFM thin films could act as materials for AFM granular recording media. We note that the AFM counterpart of the well-established granular ferromagnetic (FM) media for hard disk drives [35–37] is still missing. If available, AFM-based granular recording media should benefit from the low stray field between oppositely ordered domains and low-energy-consuming methods to switch the AFM state. A fundamental understanding of the interaction of AFM textures with grain

boundaries is needed to enable development of memory concepts based on granular AFMs.

Here, we propose a theoretical approach to describe the intergrain coupling in easy-axis AFMs. This material model allows us to predict antiferromagnetic domain patterns dependent on the material parameters. A correlation of the domain pattern with the granular film morphology provides insights into the interaction of antiferromagnetic domain walls with grain boundaries. We apply this approach to Cr_2O_3 thin films with columnar grains of lateral size of about 50 nm. Based on a fractal dimension analysis of the experimentally measured domains pattern and distribution of AFM domains by size, the intergrain nearest-neighbor exchange coupling is estimated to be about 14% of the bulk nearest-neighbor exchange coupling in Cr_2O_3. To understand the experimental domain patterns and to explain the stability of small domains with sub-100-nm dimensions, we find that the intergrain exchange parameters should possess a broad distribution and include a fraction of ferromagnetic bonds between grains. We put forth a concept of a granular AFM memory device and describe design rules for the reduction of the bit size. We show that the interbit distance can be reduced to the size of one or two individual grains without affecting the stability of neighboring bits. The proposed approach can be extended for the analysis of three-dimensional polycrystalline AFMs as well as materials with chiral and magnetoelastic contributions.

II. RESULTS

A. Granular antiferromagnetic films of Cr_2O_3

In experiments, we prepare Cr_2O_3 granular films of 200-nm thickness by reactive evaporation on *c*-cut sapphire substrates. The films exhibit columnar grains with an average lateral size, l_g, of about 50 nm and a high crystallinity within each grain [Fig. 1(a), Fig. S1 within the Supplemental Material [38]]. Grain boundaries as well as other structural defects like dislocations and vacancies [30] appear in Cr_2O_3 films grown on Al_2O_3 as a result the epitaxial strain relaxation and in-plane twinning [26]. In particular, twinning results in the rotation of grains, but not in the tilt of the *c* axis of individual grains. In Cr_2O_3, the magnetic easy axis is oriented along the *c* axis. Under this assumption, the easy axis within Cr_2O_3 grains is strictly fixed in space.

The magnetic ordering of Cr_2O_3 is described by the primary AFM order parameter [Néel vector, $\mathbf{n} = (n_x, n_y, n_z)$] defined as the staggered sum of four sublattice spins within the rhombohedral unit cell [39]. The spatial distribution of the Néel texture is primarily determined by the competition between exchange and anisotropy energies. This interplay determines the spatial extent of a magnetic texture of the order of the magnetic length, ℓ, which is about 20 nm for Cr_2O_3 at room temperature [27,40]. Accurate

up to the definition of "up" and "down" $\mathbf{n}$ domains, the Néel ordering can be associated with the uncompensated magnetization $\mathbf{m}_{surf}$ at the top surface of the film [41].

We access the real space mapping of magnetic domain patterns via scanning N-*V* magnetometry [27,28]. A typical picture of stray fields $\mathbf{B}_{N-V}$ originating from the inhomogeneous spatial distribution of $\mathbf{m}_{surf}$ is shown in Fig. 1(b). The spatial resolution of stray fields mapping is set by the standoff distance between the sensing spin and the sample and amounts to about 50 nm. We perform a reconstruction of the magnetization based on the measurement of the stray-field maps, see Fig. 1(c). For the reconstruction, we assume that the magnetization points along the *c* axis due to the anisotropy of Cr_2O_3 and is homogeneous along the sample thickness. The latter assumption is valid for the case of easy-axis high-quality crystallites where there are no thermodynamic reasons for spontaneous formation of domains within one grain [33]. Furthermore, the films in our study are rather thick and finite-size effects are not expected. To this end, we demonstrate that finite-size effects can be observed in Cr_2O_3 film with thickness of about 15 nm [15]. With the information that stray-field maps are measured in a parallel plane at the known N-*V* height of about 50 ± 5 nm, magnetization can be reconstructed [42–44]. We note that for domain sizes of the order of the N-*V* height, the determination of the fractal dimension of the domain pattered based on the reconstructed magnetization matches well with the fractional analysis based on the magnetic stray-field profile.

B. Model of a granular antiferromagnet

In the following, we develop a model for a granular AFM and apply it to Cr_2O_3 films. We note that (i) the macroscopic model of thin-film Cr_2O_3 is equivalent to a two-sublattice AFM with the easy axis of anisotropy along *c* direction [39]; (ii) magnetic stray fields between individual grains are much weaker than in ferromagnetic media and (iii) the high-quality columnar structure of films (Fig. S1 within the Supplemental Material [38]) allows us to assume a uniform $\mathbf{n}$ texture along the film thickness.

To formulate a theoretical approach for granular AFM thin films, we consider a two-dimensional bipartite AFM lattice [Fig. 1(d)]. In this case, the Néel vector $\mathbf{n}$ is given by a staggered sum of four neighboring moments whose direction (up or down) is marked by red and blue color, see Fig. 1(d) [45]. Boundaries between grains in such AFMs can be considered as a magnetic material in a state with a potential presence of FM and AFM exchange bonds. These boundaries are simulated via changing the single-ion anisotropy $|K_b^i| \leq K_g$ at the *i*th site adjacent to the grain boundary and exchange bonds $|J_b^{ik}| \leq J_g$ between *i*th and *k*th sites, with K_g and J_g being the nominal values within grains. In the following, indices indicating lattice sites will be omitted for simplicity. We consider cases when the
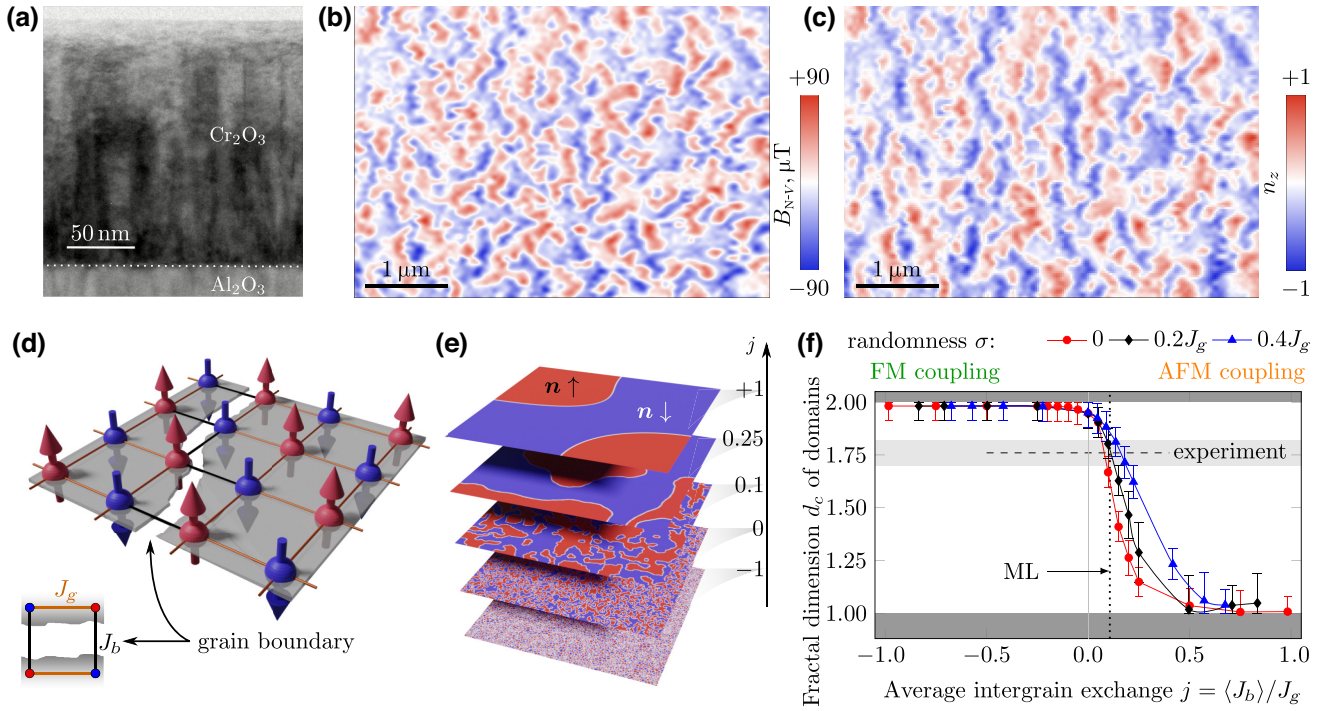
FIG. 1. Granular antiferromagnetic thin film. (a) Transmission electron microscopy image of a 200-nm-thick Cr_2O_3 film. (b) Mapping of magnetic stray fields of the thin-film sample at room temperature using scanning nitrogen-vacancy (N-V) magnetometry. (c) The map of the surface magnetization along the c axis, which is associated with the out-of-plane component of the Néel vector **n** and scaled to the range of $[-1, 1]$. The map of the surface magnetization corresponds to the map of magnetic stray fields shown in (b). (d) Schematics of the grain boundary used in the theoretical model: the intragrain exchange J_g (orange bonds) is the same for all neighboring spins within the grain. The grain boundary is characterized by the intergrain exchange J_b (black bonds). (e) Set of equilibrium domain patterns simulated for different values of $j = \langle J_b \rangle / J_g$ and $\sigma = 0$. Color indicates the out-of-plane component of the Néel vector **n**. (f) Fractal dimension d_c of the simulated AFM domain patterns as function of intergrain exchange. Symbols correspond to simulations. Lines are guides to the eye. Horizontal gray-shaded region indicates the range of d_c obtained from the analysis of the antiferromagnetic domain pattern measured using scanning N-V magnetometry [panel (b)]. The dotted line indicates estimation of j obtained using machine learning (ML).

material at grain boundaries has either the same magnetic parameters as within the sample or assign magnetic parameters to different lattice sites according to truncated normal distributions with the given center, average, and standard deviation. The position of grain boundaries is determined by the Voronoi tessellation [46] of the lattice consisting of 1500×1500 magnetic sites. The magnetic length set to $\ell = 5a$ with a being the lattice spacing is used to keep sufficiently high resolution for the numerical analysis.

We perform a set of spin-lattice simulations considering relaxation dynamics in scope of the Landau-Lifshitz-Gilbert equation with different material parameters at grain boundaries and geometrical parameters of grains. An exemplary set of equilibrium states is shown in Fig. 1(e), where the intergrain exchange ratio $j = \langle J_b \rangle / J_g$ with $\langle \bullet \rangle$ indicating average, is varied between the limiting cases of fully AFM and fully FM exchange bonds. To compare the experimental and simulated domain patterns, machine learning (ML) with the neural-network topology ResNet18 is used [47]. This allows us to obtain the best *visual* match

between simulations and experimental data, which occurs at $j \approx 0.11$ and standard deviation $\sigma \approx 0.16$ and with a constant anisotropy over the sample.

To understand the physical picture behind this ML prediction, we utilize a complementary approach based on the determination of the Minkovski-Bouligand fractal dimension [48–53], which reads

$$d_c = \lim_{\epsilon \to 0} \frac{\log N(\epsilon)}{\log \frac{1}{\epsilon}}, \quad (1)$$

where N is the number of squares, which cover domain-wall lines and ϵ is their lateral size. An increase of d_c in the range $d_c \in [1, 2]$ corresponds to the change of the shape of the domain walls from straight (or weakly curved) to space-filling curves, which densely cover the entire field of view. We binarize the experimentally measured N-V maps [Fig. 1(b)] to localize domain walls as a boundary between regions of different color. The experimental maps exhibit a self-similarity behavior at spatial scales larger than a few

hundred nanometers. This gives $d_c^{\text{N-}V} = 1.76 \pm 0.06$, see light-gray region in Fig. 1(f).

To determine an appropriate model of AFM granular media based on Cr_2O_3 thin films, we consider the change of material parameters at boundary sites. This includes the variation of the inter-grain exchange characterized by the pair (j, σ) and anisotropy at boundary sites.

The simplest realization of this model is represented by the intragrain exchange J_g and intergrain exchange J_b for any pair of boundary magnetic sites and constant anisotropy coefficient at each site, see red line ($\sigma = 0$) in Fig. 1(f). We consider the evolution of the domain pattern with the change of the parameter j, see Figs. 2(a)–2(e). For $j \gtrsim 0.5$, domain walls reveal a single-crystal-like behavior with $d_c \approx 1$, see Figs. 1(f) and 2(e). This state corresponds to the presence of large domains of the order of the sample size. The monodomain state can be reached with longer simulation time, which is evident from the comparison

of the relaxation dynamics for different models (Fig. S2 within the Supplemental Material [38]). Taking smaller but still AFM values of j, the fractal dimension rapidly grows approaching $d_c \approx 1.95$ for magnetically decoupled grains (at $j = 0$). The respective domain pattern increases its segmentation, see Fig. 2(b). The ferromagnetic intergrain coupling with $j < 0$ makes the system frustrated with the maximal $d_c \approx 1.98$, see Fig. 2(a). In this case, domains are located at individual grains. The size of structural grains determines the saturation value of d_c, which is reached for $j \lesssim -0.15$.

Furthermore, we consider a more complex model of random intergrain exchange coupling with a finite σ, see black and blue curves in Figs. 1(f) and 2(f)–2(j). The randomness of the exchange coupling shifts the curve $d_c(j)$ towards higher fractal dimensions in the transition region from the single-crystal-like to the frustrated behavior, see black and blue curves in Fig. 1(f). This is determined by the increase in the proportion of weaker AFM and FM bonds, while
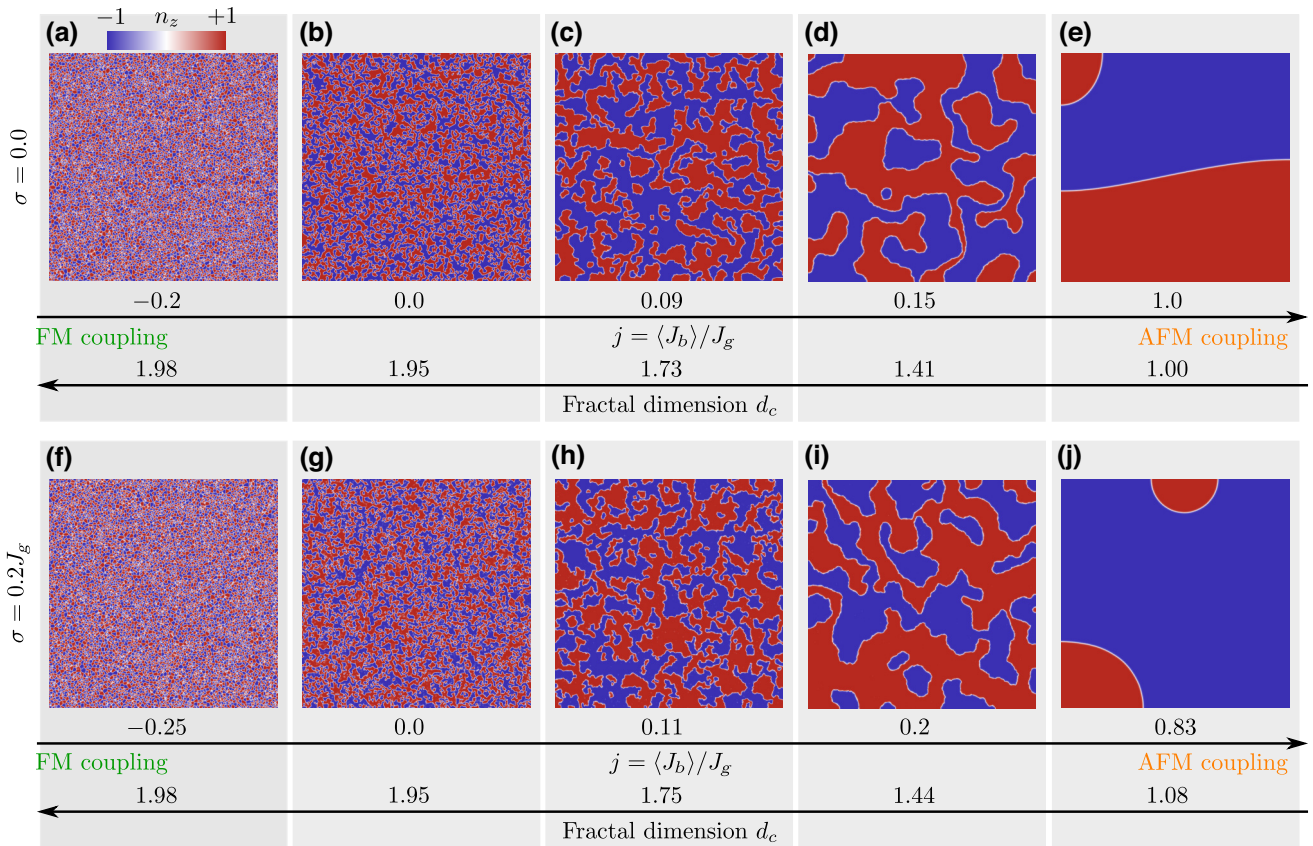

FIG. 2. Domain-wall patterns obtained for the variation of the exchange bonds at grain boundaries. Here, anisotropy is kept constant ($K^i \equiv K_g$) for all sites. In (a)–(e), the exchange constant $|J_b| \leq J_g$ is the same at all boundary sites. In (f)–(j), values of J_b are distributed according to the truncated normal distribution with the given average and standard deviation σ. In each panel, we show the domain pattern calculated for the indicated j and the corresponding fractal dimension, d_c, of the domain pattern. The images shown in (a)–(e) correspond to the red curve in Fig. 1(f). The images shown in (f)–(j) correspond to the black curve in Fig. 1(f). Domain patterns for the curve with $\sigma = 0.4 J_g$ are shown in Fig. S13 within the Supplemental Material [38].
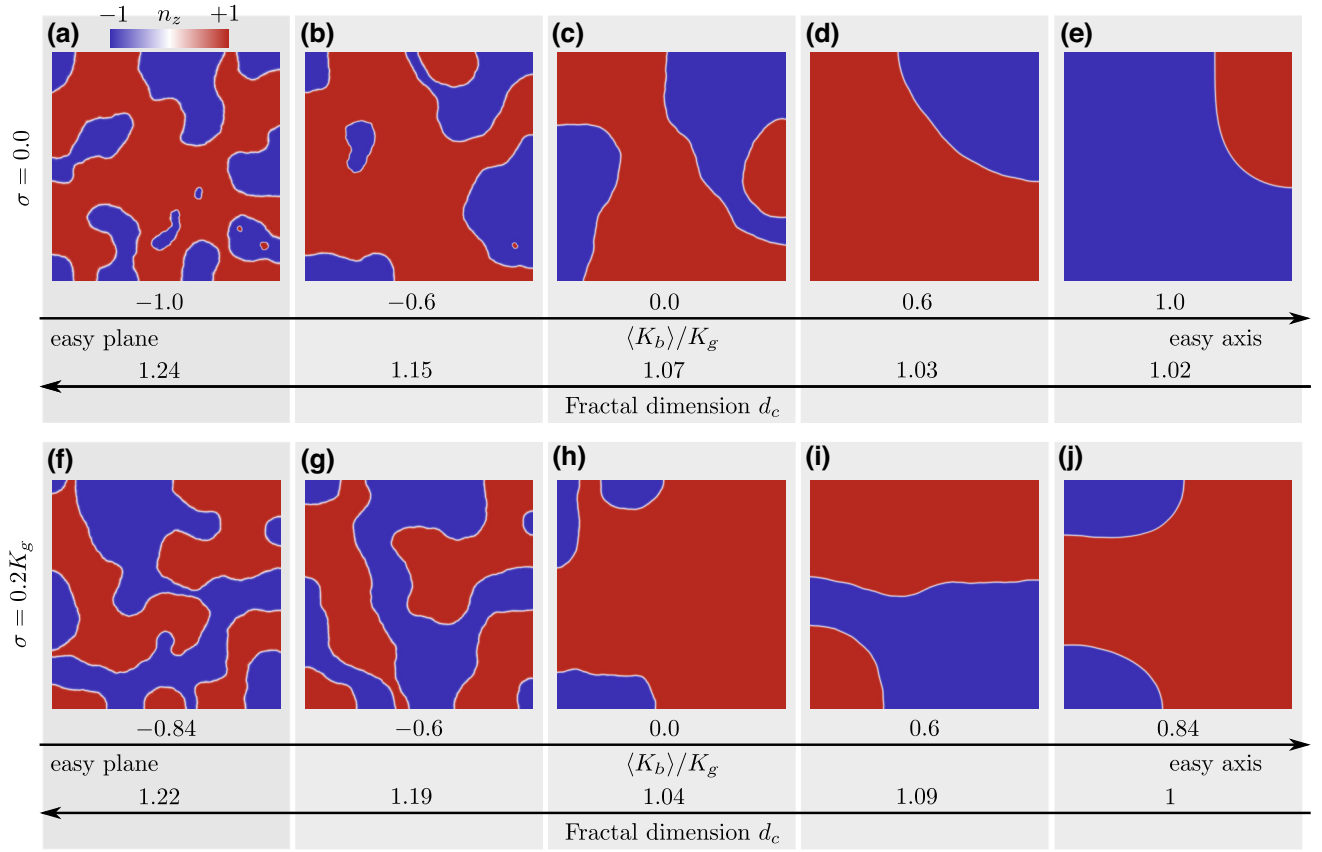
FIG. 3.   Domain-wall patterns obtained for the variation of the anisotropy at grain boundaries. Here, all exchange bonds are kept constant ($J^{ik} \equiv J_g$). In (a)–(e), the anisotropy coefficient $|K_b| \leq K_g$ is the same at all boundary sites. In (f)–(j), values of K_b are distributed according to the truncated normal distribution with the given average and standard deviation σ. In each panel, we show the domain pattern calculated for the indicated averaged anisotropy coefficient and the corresponding fractal dimension, d_c, of the domain pattern. In contrast to the case of the exchange-variation-driven coupling between grains shown in Fig. 2, here we do not observe strong stability of domain walls (Fig. S2 within the Supplemental Material [38]). Furthermore, the maximal value of d_c is smaller than the one observed experimentally.

strong AFM intergrain bonds do not play a significant role in the pinning of domain walls. For $j \lesssim 0$ the quantitative behavior of the domain pattern is the same and independent of σ. In this way, the value of $d_c^{\text{N-}V}$ corresponds to the interval $0.07 \leq j \lesssim 0.25$ with the boundaries determined by the variation of σ from 0 to the uniform distribution. In this respect, analysis of the self-similarity of the domain pattern can be used to estimate the mean value of the intergrain exchange coupling constant.

Following the same procedure, we consider influence of the variation of the anisotropy at the grain boundaries keeping the exchange bonds equal to the bulk value J_b everywhere. This gives fractal dimension in the range of $d_c^{\text{ani}} \in [1, 1.3]$ (Fig. 3), which is smaller than the experimentally determined $d_c^{\text{N-}V}$. This is caused by the broadening of the domain-wall width with the decrease of K_b. In turn, broader domain walls require wider grain-boundary regions to act as a decisive factor for the pinning of antiferromagnetic domain walls. Therefore, as the material

model we chose a medium with an inhomogeneous spatial distribution of the strength of exchange bonds and assume the same anisotropy $K_i = K_g$ everywhere, including grain-boundary sites.

C. Appearance of small domains

The experimentally observed fractal dimension $d_c^{\text{N-}V}$ can be obtained in a wide range of values of the width of the intergrain coupling distribution, σ, see Fig. 1(f). To determine the value of σ, we rely on the statistics of the domain distribution by size. Figure 4(a) shows examples of representative small-sized domains detected by the scanning N-V magnetometry in our samples. The domain size is measured in units of the average grain area $S_{\text{av}} = l_g^2$. We note the irregular shape of domains with the area of several S_{av}, which may be caused by the pinning of antiferromagnetic domain walls on individual grains or only a few neighboring grains. The size distribution of the small-sized
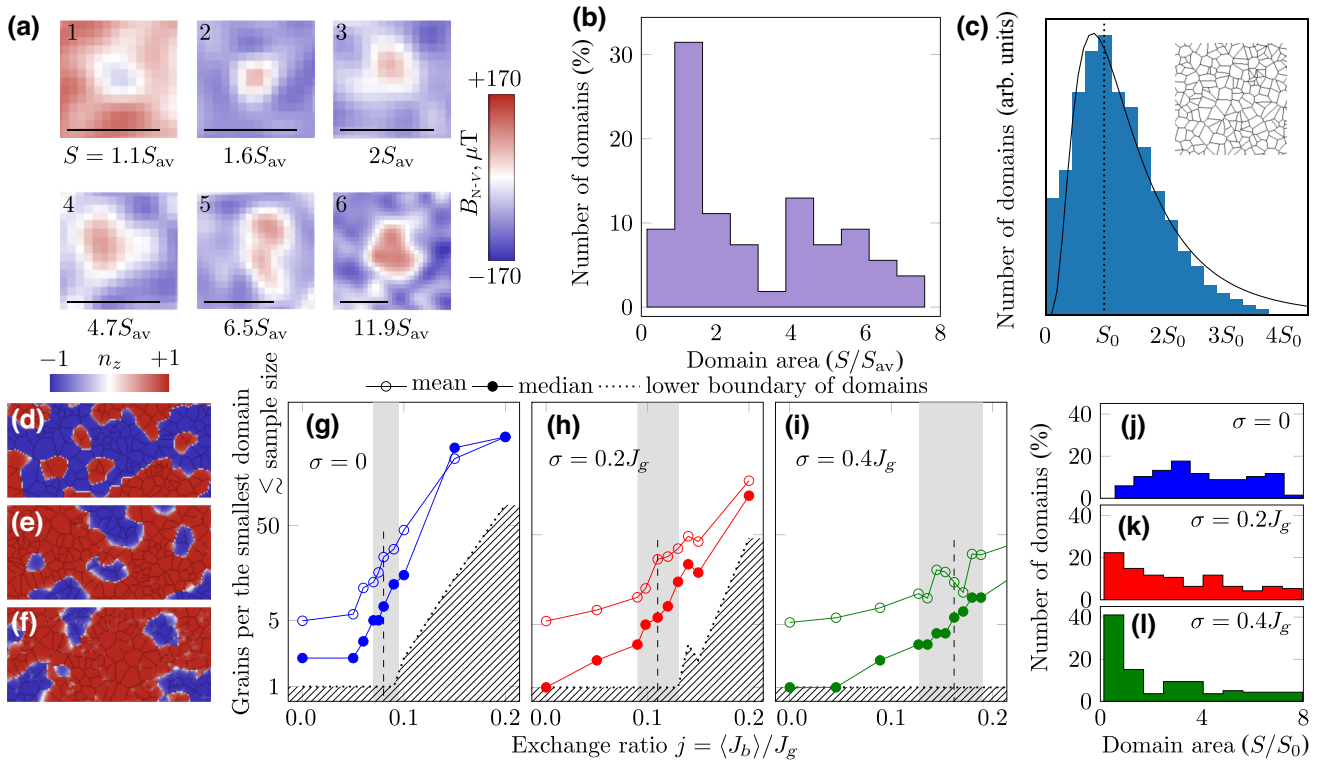
FIG. 4.   Statistics of small-sized domains. (a) Representative images of small-sized domains obtained by scanning N-V magnetometry. Areas S of the shown domains are labeled in units of the average grain area $S_{av} = l_g^2 \approx 2500$ nm^2. All scale bars: 250 nm. (b) The distribution of domains by size extracted based on the analysis of the experimentally measured domain patterns. The analysis is done over the area of 54 µm^2. (c) The distribution of grain sizes in simulations with S_0 being the mean value. Inset shows the typical grain pattern used in simulations. Solid line represents a fit by log-normal distribution. (d)–(f) Exemplary domain patterns superimposed with grains are simulated for pairs of (j, σ): (d) (0.08, 0), (e) (0.11, $0.2J_g$), and (f) (0.162, $0.4J_g$). Grain boundaries are marked by gray lines. (g)–(i) Size of small-sized domains extracted from simulated domain patters. The simulations are done for different intergrain exchange J_b and dispersion σ. Open and closed symbols indicate mean and median domain size, respectively. Lines are guide to the eye. Gray region corresponds to the values of j giving the fractal dimension comparable with the experimental one, see Fig. 1(f). The shaded area below the dotted line indicates domain sizes, which are not observed in simulations for the given j and σ. Vertical dashed lines correspond to j, for which the domain pattern is shown in (d)–(f). (j)–(l) Representative examples of distributions of small-size domains by size for values of j marked by vertical dashed lines in (g)–(h) and domain patterns in (d)–(f).

domains, which are accessed by N-V magnetometry, is bimodal (with two peaks) with maxima at a single grain and five grains, see Fig. 4(b).

Spin-lattice simulations allow the shape of AFM domains and grains to be matched unambiguously. A typical log-normal-like distribution of grain sizes [54] in simulations is shown in Fig. 4(c), where we define S_0 as the most probable area of a grain. The smallest domains in units of S_0 are always located at single grains, see also examples of rounded and elongated domains in Figs. 4(d)–4(f). Figures 4(g)–4(i) show the number of grains per domain for different j and σ. While the magnetically decoupled grains reveal a single-grain domain pinning as a common behavior [e.g., more than half of studied domains occupy ≤ 2 grains for $(j, \sigma) = (0, 0)$], the value of the median shifts towards larger domains for stronger coupling. For $\sigma = 0$, domains become comparable to the sample size already at j approximately 0.15

[Fig. 4(i)]. This is in contrast to the finite-width distributions of J_b, which include frustrated bonds. Larger values of σ lead to the stabilization of single-grain domains even at j approximately 0.2 [Figs. 4(e) and 4(h)].

Representative distributions of domains by size and a match of the AFM texture with grains are shown in Figs. 4(j)–4(l), see also Figs. S3–S5 within the Supplemental Material [38]. The bimodal behavior is observed for the case of magnetically decoupled grains ($j = 0$ and $\sigma = 0$) and for the case of sufficiently large σ approximately 0.3 [Figs. 4(k) and 4(l)]. At the same time, the bimodal distribution for $j > 0$ and $\sigma = 0$ does not match the experimental observations due to the low probability of single-grain domains with $S \approx S_0$. We note that the exclusion of the ferromagnetic intergrain exchange bonds leads to a significant reduction of $d_c < d_c^{N\text{-}V}$ indicating their significance for the recovering of the experimentally observed domain patterns. The analysis of the size distribution of

small-sized domains in the antiferromagnetic domain pattern provides access to the distribution of the inter-grain exchange coupling parameters, σ.

D. Pinning of domain walls

The pinning behavior for domain walls is determined by their energy profile. The established micromagnetic models predict the pinning of topologically nontrivial texture ends at structural defects such as dislocations [17,55–58], which also allow the presence of disclinations in

(a)

Regular domain wall (b)

Boundary domain wall (c)

(b)

Domain 1   Domain wall   Domain 2

(c)

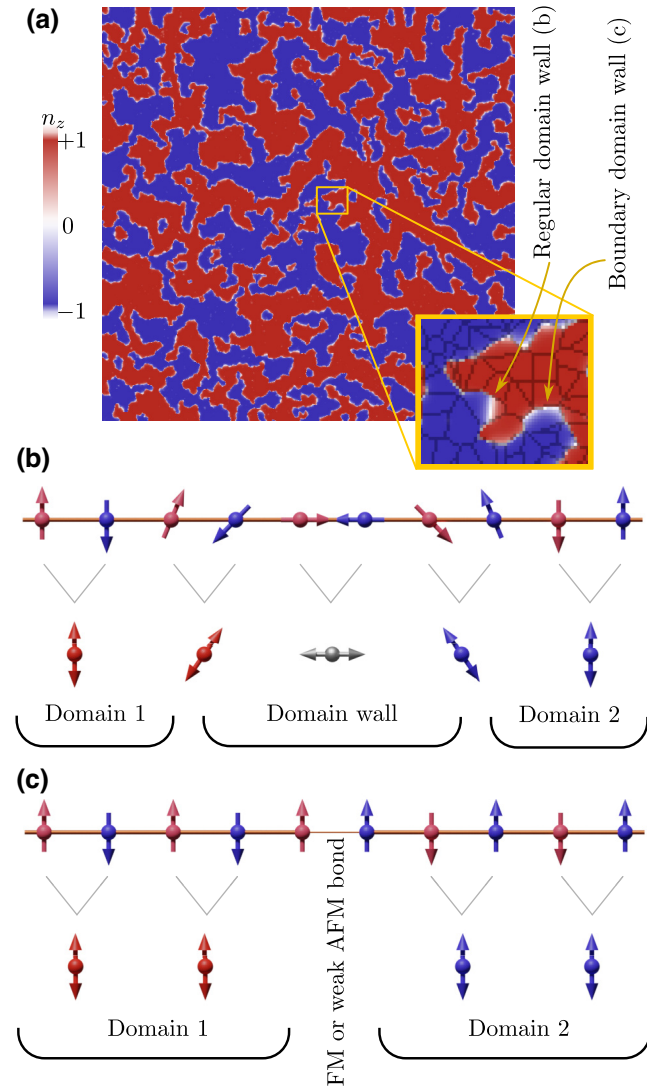FM or weak AFM bond

Domain 1   Domain 2

FIG. 5. Pinning of antiferromagnetic domain walls on grain boundaries. (a) Domain pattern with $d_c = 1.74$ obtained in spin-lattice simulations ($j = 0.12$, $\sigma = 0.2J_g$). Color indicates the direction of the out-of-plane component of the Néel vector **n**. Inset shows two types of domain walls: regular wall (gradual transition between red and blue colors), which crosses the grain, and narrow boundary domain wall appearing at grain boundaries only (gray lines). Schematics of the regular (b) and boundary (c) domain walls in terms of spins (top row in each panel) and Néel vectors (bottom row in each panel).

the magnetic ordering in addition to domain walls. This pinning mechanism is of strong relevance for *easy-plane* AFMs. Within the σ model, dislocation lines perpendicular to the easy axis in biaxial AFMs form a 180° domain wall [58]. Higher-order anisotropies allow for the formation of the domain structure with defects in the crystal and the vector field **n**(**r**) located within the domain walls [17]. Effects of microtwins in such tetragonal AFMs as Cu-Mn-As can be effectively described by the anisotropy field associated with the rotation of easy planes at the microtwin and strain fields contributing to the magnetoelastic energy [59]. Similar studies for easy-axis AFMs are missing.

Figure 5(a) shows an example of two types of domain walls observed in simulations, which are stabilized in samples with grain boundaries and out-of-plane easy-axis magnetic anisotropy. Each domain wall consists of intermittent regions of different structure, which are shown schematically Figs. 5(b) and 5(c). The stabilization of the AFM texture happens via pinning of narrow domain walls along grain boundaries, which are labeled as boundary domain walls in Fig. 5(a). Their width is significantly smaller than the magnetic length and is similar to the width of the grain boundary for the case of FM intergrain exchange bonds. At the joint points of separate grains, the boundary walls either bend along the grain boundary or continue as a regular domain wall of bulklike width across a grain. The regular domain wall keeps the Néel vector of constant length [Fig. 5(b)]. In contrast, boundary domain walls have reduced width due to the lowering of the effective AFM exchange interaction at the grain boundary or presence of frustrated bonds with FM coupling, which favors antiphase AFM domains in the neighboring grains [Fig. 5(c)]].
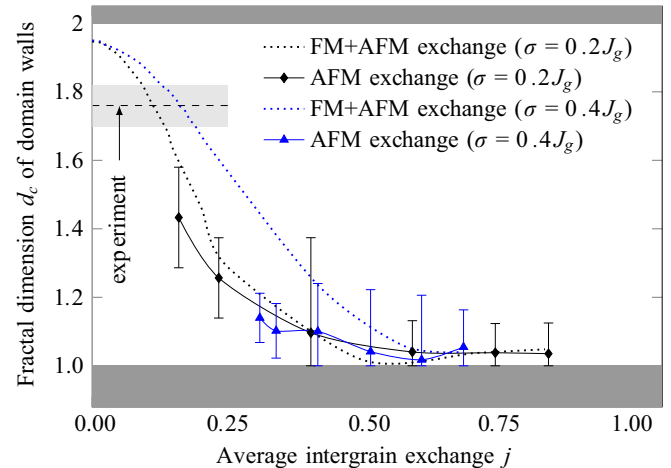
FIG. 6. Comparison of fractal dimensions of domain patterns. Fractal dimension of domain patterns are calculated for the case of purely AFM coupling between grains and compared with the case of full-range distribution of exchange bonds. The dotted lines repeat $d_c(j)$ for $\sigma > 0$ shown in Fig. 1(f) for comparison.

To illustrate the relevance of even a small fraction of FM intergrain coupled bonds, we perform simulations with the truncated normal distribution limited to the range of $j \in [0, 1]$, see Fig. 6. The resulting maximal value of d_c is approximately 1.4, which is significantly lower than d_c^{NV}. We note that the presence of FM exchange bonds leads to a strong intergrain coupling.

Grain-boundary-induced pinning of small domains can be utilized for the realization of an AFM counterpart of granular recording media [Fig. 7(a)]. For a sample with a random placement of grains, the success in writing of a single bit is determined by the stability of the locally defined magnetic state with the reversed orientation of the order parameter. We consider the stability of circular bits varying their size and density in Figs. 7(b) and 7(c). We

note that in Fig. 7(a) bits are rectangular and positioned right next to each other. In Figs. 7(b) and 7(c), written "red" domains are round and there is spacing between them. In our study, we tune the spacing to understand stability of the written domains.

To emulate writing of the bits, we define the initial state with the opposite ordering of the sublattice magnetic moments within circular regions and allow the system to relax with large Gilbert damping. For the intergrain coupling parameters estimated for our Cr_2O_3 thin films [green triangles with dotted lines in Figs. 7(d) and 7(e)], the smallest bits satisfying high values of writing success require at least ten grains. This is comparable with domains shown in N-V magnetometry with a lateral size of about 200 nm (about 10–15 grains), see inset in Fig. 7(a).
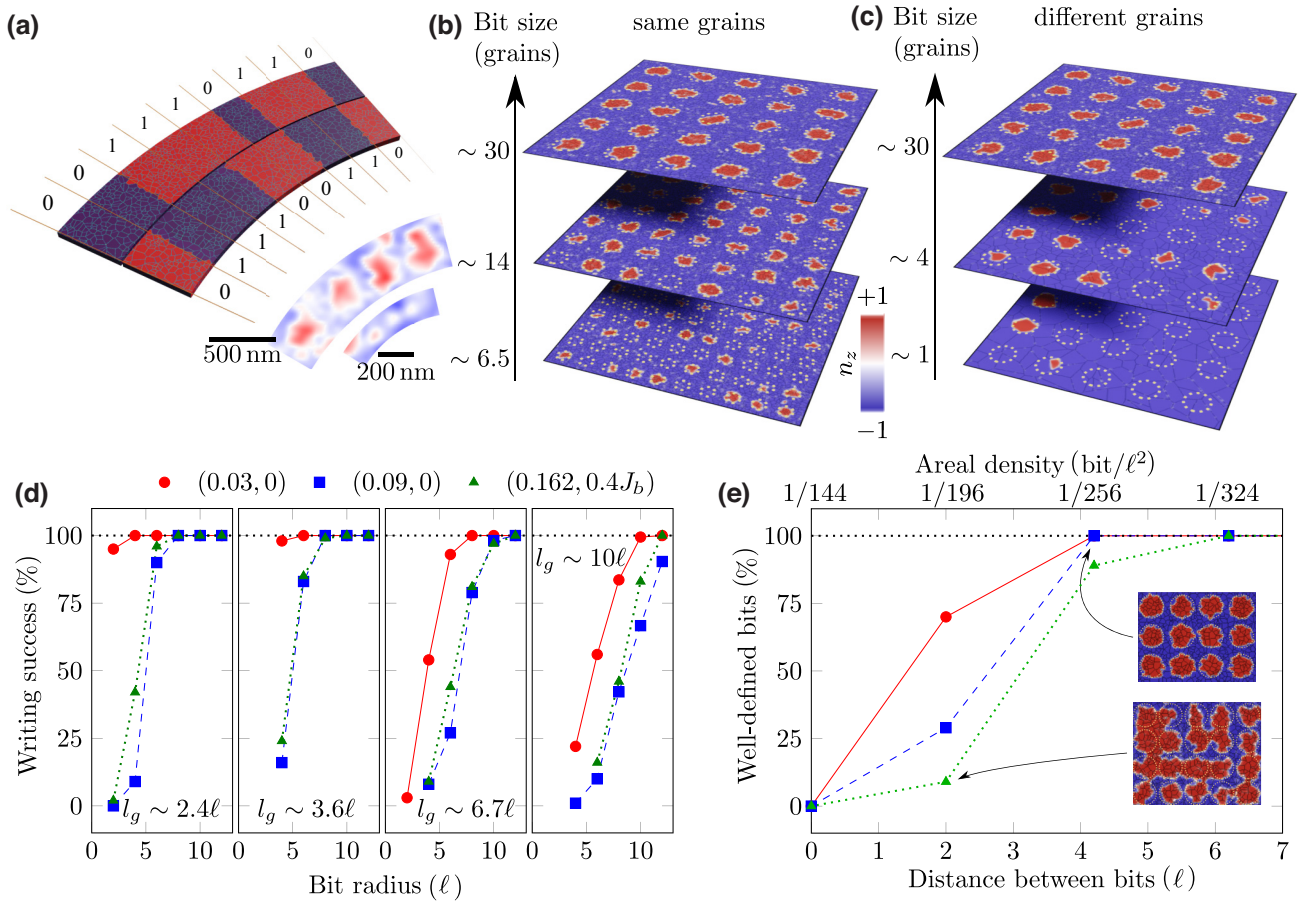

FIG. 7.   Concept of AFM granular recording media. (a) Schematics of the AFM granular recording media. Red and blue colors represent opposite directions of the AFM order parameter **n** within domains, separated by domain walls. Inset shows two image sequences of small-sized domains taken from the scanning N-V microscopy data [Fig. 1(a)], which mimic bit tracks shown in (a). (b) Bits "1" (red) written to the state "0" (blue) in a granular film with an average grain size of about 2.3ℓ of different radius and spacing equal to the bit diameter. Dotted circles indicate writing area. Grain boundaries are shown by gray lines. Depending on the bit size, there are successful and failed writing attempts. (c) Same as in (b) but for different granularities and the same bit radius. (d) Percentage of successfully written bits for a single writing attempt depending on the bit size and size of grains l_g. Symbols correspond to the different intergrain coupling, lines are a guide to the eye. (e) Percentage of well-defined bits with radius of 6ℓ (corresponding to at least 90% of writing success) depending on the separation distance between bits. The color of symbols corresponds to the legend in (d). Insets show examples of poor- (bottom) and well-defined (top) states.

For the Cr_2O_3 samples fabricated in this work with a grain size of 50 nm and bit consisting of ten grains, the bit areal density can reach about 4 Gbit/inch^2. The areal density can be increased for samples with smaller grain sizes and optimized intergrain coupling, i.e., approaching $j \to 0$ and $\sigma \to 0$ avoiding the appearance of ferromagnetic intergrain bonds [red symbols with solid lines in Figs. 7(d) and 7(e)]. For the random grain pattern, all written bits are well defined if separated at least by two grains of the average size [Fig. 7(e)] independent of the intergrain coupling. However, weaker j and σ promote better bit shapes at smaller distances. For example, 1 Tbit/inch^2 can be achieved for antiferromagnetic thin films with the grain lateral size of $l_g = 3$ nm and weak intergrain coupling: small but positive j and absence of ferromagnetic intergrain bonds, which requires $\sigma \to 0$. We note that grains with $l_g < \ell$ do not support regular domain walls, which enhances stability of single-grain domains.

III. DISCUSSION

In summary, we develop a model of a granular AFM thin film with out-of-plane easy-axis anisotropy and apply it to Cr_2O_3. The experimentally observed domain patterns are recovered by the distribution of exchange bonds at grain boundaries with a weak antiferromagnetic average (up to 0.14 of the nominal value) and wide standard deviation (about $0.4 J_g$). The presence of ferromagnetic exchange bonds at grain boundaries is found to be the key factor responsible for the strong domain-wall pinning.

Therefore, an insight into the intergrain exchange in granular thin-film antiferromagnets can be achieved solely based on the statistical analysis of measured AFM domain patterns. These parameters are crucial to calibrate the theoretical model for prospective predictive analysis of the domain patterns and their evolution in granular AFM thin films.

We demonstrate a straightforward route to validate the material model experimentally by relying on imaging of antiferromagnetic domain patterns. While the analysis of the fractal dimension provides access to the strength of the intergrain exchange, the size distribution of small-sized domains allows us to estimate the width of the distribution of the exchange coupling constants at grain boundaries.

In our work, we perform imaging of antiferromagnetic domains at nano- and microscale using scanning N-V magnetometry. However, other visualization methods to image-domain patterns at high spatial resolutions can be applied including electron-based [60] and x-ray-based [52, 61,62] microscopies (for a review see Ref. [63]). Depending on the complexity of the experimentally determined domain patterns, the use of machine-learning schemes offers quick access to relevant material parameters, which can then be used for an in-depth theoretical analysis.

The presented results should stimulate further fundamental activities on determining the material parameters of granular antiferromagnets at the nanoscale and understanding the role of finite-size effects with different types of intergrain coupling. Furthermore, the design of grain boundaries (e.g., twin boundaries) can become an efficient control parameter of antiferromagnetic domain patterns at the nanoscale. Our approach can be applied to other types of granular and three-dimensional polycrystalline AFMs. We anticipate that it would be relevant to extend this model to account for (i) strain effects, (ii) easy-plane antiferromagnets, (iii) metallic antiferromagnets. In these systems, the physical mechanism of the intergrain coupling could require other atomistic models. The description of the strain-mediated domain formation in such materials as Fe_2O_3 or NiO needs development of either spin lattice or micromagnetic model of strain in numerics. For the case of chiral and magnetostrictive materials, the model can be extended by taking into account the Dzyaloshinskii-Moriya interaction and strain fields created by microtwin and other types of defects [59].

Furthermore, the ability to obtain a predictive model of a granular uniaxial AFM thin film enables activities on AFM memory concepts. Indeed, our theoretical approach provides design rules for the development of granular AFM memory devices. Tuning the grain size, bit size, and material parameters to eliminate bulklike domain walls, may allow us to reach a bit areal density up to 1 Tbit/inch^2. Further improvement towards single-grain bit operations is related to the design of the regular grain pattern making an AFM analog of bit-patterned magnetic recording.

For the specific case of c-plane Cr_2O_3, the magnetic state is independent of atomic steps [41]. This implies that the orientation of the Néel vector is uniquely determined within the domain, independently of structural imperfections on the surface. We anticipate that the readout of information bits can be done based on N-V magnetometery integrated in a read head instead of the currently used magnetoresistive sensor element. Furthermore, we note that there are reports on the use of magnetic force microscopy in the magnetoelectric mode to readout magnetic state of Cr_2O_3 samples [64]. In addition to the force microscopy methods, it is possible to envision that Cr_2O_3 could be integrated in magnetoelectric RAM cells [25,26,65,66], which allows the magnetic state to be readout electrically. We note that there are recent demonstrations of the possibility to reorient the Néel vector in Cr_2O_3 by applying electric fields only [14]. The means on how to efficiently write bits of information in granular Cr_2O_3 media remains to be explored. Considering that the order parameter of Cr_2O_3 thin films can be switched magnetoelectrically [26] and even relying on electric fields only for the case of B-doped Cr_2O_3 [14], granular AFM media based on Cr_2O_3 can be potentially more energy efficient than the contemporary concepts based on magnetic field writing into

ferromagnetic media [66]. Still, the fundamentals on the dynamics of the order parameter written with electric fields or magnetoelectrically for insulating granular Cr_2O_3 thin films are to be explored. Hence, we expect that our work will stimulate further activities on the theoretical and experimental studies of ultrafast switching processes (including THz dynamics [67–69]) in antiferromagnetic materials.

APPENDIX A: THIN-FILM FABRICATION AND STRUCTURAL CHARACTERIZATION

We prepare 200-nm-thick Cr_2O_3 thin films on c-cut single-crystal $Al_2O_3(0\,0\,0\,1)$ substrates (Crystec GmbH) by reactive evaporation of chromium at $700\,°C$ with a background partial pressure of molecular oxygen of 10^{-5} mbar (base pressure below 10^{-7} mbar; deposition rate of about 0.04 nm/s; source-to-sample distance, 60 cm). After the deposition of Cr_2O_3, the samples are heated up to $750\,°C$ for several minutes to improve the surface quality of the thin film. Afterwards, the substrate is cooled down by the heat dissipation through the sample mounting structure.

Cross-section bright-field TEM and HRTEM analysis [see Fig. 1(a) and Fig. S1 within the Supplemental Material [38]] is performed using an image-C_s-corrected Titan 80-300 microscope (FEI) operated at an accelerating voltage of 300 kV. Prior to TEM analysis, the specimen is mounted in a double-tilt low-background holder and placed for 8 s into a Model 1020 Plasma Cleaner (Fischione) to remove potential contaminations. Classical TEM cross sections, glued together in face-to-face geometry using G2 epoxy glue (Gatan), are prepared by sawing (Wire Saw WS 22, IBS GmbH), grinding (MetaServ 250, Bühler), polishing (Minimet 1000, Bühler), dimpling (Dimple Grinder 656, Gatan), and final Ar ion milling (Precision Ion Polishing System PIPS 691, Gatan).

Figure S1(a) within the Supplemental Material [38] shows an overview bright-field TEM image of the 200-nm-thick granular Cr_2O_3 film deposited onto a c-cut sapphire substrate. Within this micrograph, the position of the TEM image depicted in Fig. 1(a) is marked with a

white-dashed square. A representative HRTEM image of the Cr_2O_3/Al_2O_3 interface is given in Fig. S1(b) within the Supplemental Material [38]. As confirmed by fast Fourier transformation (FFT) of the substrate region [Fig. S1(c) within the Supplemental Material [38]], the sapphire is in $[1\,0\,0] = [2\,\bar{1}\,\bar{1}\,0]$ zone axis orientation for the particular TEM lamella. In the sample region shown in Fig. S1(b) within the Supplemental Material [38], the Cr_2O_3 film grows epitaxially on the $Al2O_3$ substrate, as confirmed by a comparable FFT of the chromium oxide presented in Fig. S1(d) within the Supplemental Material [38]. Only a few misfit dislocations, whose positions are marked with white circles in Fig. S1(b) within the Supplemental Material [38] are present directly at the Cr_2O_3/Al_2O_3 interface. A representative HRTEM image of the sample surface region is given in Fig. S1(e) within the Supplemental Material [38]. Regarding the Cr_2O_3 film, there are two superimposed grains. While the FFT of the left image part in Fig. S1(f) within the Supplemental Material [38] can be described by a pattern in $[1\,0\,0]$ zone axis geometry [as in Figs. S1(c) and (d) within the Supplemental Material [38]], the FFT of the middle image part in Fig. S1(g) within the Supplemental Material [38] is caused by superposition of a grain in $[1\,0\,0] = [2\,\bar{1}\,\bar{1}\,0]$ zone axis orientation and a grain in $[1\,1\,0] = [1\,1\,\bar{2}\,0]$ zone axis geometry, i.e., rotated by $60°$ in plane to the neighboring grain.

APPENDIX B: SCANNING N-V MAGNETOMETRY

Scanning N-V magnetometry [71] is performed under ambient conditions at about $22\,°C$. The sensor tips are fabricated from single crystal, $\langle 100 \rangle$-oriented diamond that is implanted with ^{14}N ions at 12 keV and annealed to form N-V centers. After lithographic fabrication, the resulting diamond scanning probe contains a single N-V center, located at the tip of a cylindrical pillar, and provides a spatial resolution of approximately 50 nm [72] and typical sensitivities of approximately $5\ \mu T/\sqrt{Hz}$ [72]. Imaging of the local stray fields is performed using dual-iso-B imaging [71] and feedback to lock to one of the N-V resonances [73]. To obtain a sign-sensitive measurements of stray fields, a small bias magnetic field of about 50 Oe is applied along the N-V axis during all measurements. The single-pixel integration time for the presented measurements range from 0.6 to 7 s.

Because of the alternating magnetic sublattices and respective compensation of the dipolar fields at the atomic level, the stray fields arising at sample surfaces [28], sample interior [15], and defects in AFMs [26,74] are usually considered to be of higher-order corrections to theoretical models. For Cr_2O_3 films considered in this work, the main source of stray fields are ferromagnetically ordered spins at the top and bottom film interfaces with the magnetic moment density $\rho = 2.4\mu_B/nm^2$ with μ_B being the Bohr magneton [15,28]. In this work we estimate the relevance

of the magnetostatic intergrain coupling as follows. The magnetic moment on the grain interfaces is of the opposite direction (e.g., upward at the top surface and downward at the bottom one) [41], which provides a partial compensation of stray fields. For a film with a thickness of 200 nm and lateral grain size of $l_g = 50$ nm (area $S_{av} = 2500$ nm^2), the strongest interaction can be between the spins of the neighboring grains at the same film interface. Considering them as elementary magnetic dipoles with moments $\mu = \rho S_{av}$ and distance $r = l_g$, the energy of their interaction is equivalent to 0.2 K in units of temperature. This is also comparable with the energy of such a dipole being exposed to a magnetic field of order of 100 μT [Fig. 1(b)]. In this estimation, we assume a checkerboard ordering of spins at the side walls of grains with the compensation of their stray fields. Thus we conclude that the influence of stray fields in our samples on intergrain coupling can be neglected for this work because the theoretical model is discussed for samples magnetically characterized at room temperature.

APPENDIX C: SPIN-LATTICE SIMULATIONS

To emulate the structure of granular thin films, we generate a Voronoi pattern using randomly placed nodes with uniform distribution within the film plane [46], see Fig. 1(d).

Magnetic sites, neighboring to the edges of the Voronoi pattern, are marked as boundary spins. Magnetic parameters of the boundary spins are changed in spin-lattice simulations aiming to identify the model of the material. We keep the magnetic moment of spins unchanged within the sample (grains and grain boundaries). Furthermore, the magnetic parameters like exchange interaction and anisotropy for each grain are kept the same. The magnetic parameters at grain boundaries (strength of exchange and its distribution as well as anisotropy) are modified. For instance, Fig. 1(d) shows the intragrain and intergrain exchange bonds, which are marked by orange and black lines, respectively.

We consider a two-dimensional antiferromagnetic bipartite lattice with square cells of 1500×1500 spins. The magnetic energy of the system is given by the anisotropic Heisenberg Hamiltonian

$$\mathcal{H} = -\frac{S^2}{2}\sum_{i,k} J_{ik}\mathbf{m}_i \cdot \mathbf{m}_j - \frac{S^2}{2}\sum_i K_i m_{iz}^2, \quad \text{(C1)}$$

where J_{ik} is the exchange integral between ith and kth spins, index k runs over the nearest neighbors, S is the spin length, $\mathbf{m}_i = (m_{ix}, m_{iy}, m_{iz})$ represents the unit vector of magnetic moment for ith site and K_i is the coefficient of the easy-axis anisotropy for ith spin. Equilibrium magnetic textures are addressed by solving the

Landau-Lifshitz-Gilbert equation

$$\frac{d\mathbf{m}_i}{dt} = \frac{1}{\hbar S}\mathbf{m}_i \times \frac{\partial \mathcal{H}}{\partial \mathbf{m}_i} + \alpha_G \mathbf{m}_i \times \frac{d\mathbf{m}_i}{dt}, \quad i = \overline{1, \mathcal{N}}, \quad \text{(C2)}$$

with $\hbar$ being the Planck constant, α_G being the Gilbert relaxation parameter and $\mathcal{N}$ being the total number of spins. The system of Eq. (C2) is solved using spin-lattice simulator SLaSi with GPU (graphics processing unit) acceleration [75]. In simulations, we set $J_g = -2.34 \times 10^{-20}$ J [76], which is close to the bulk nearest-neighbor exchange integral. The anisotropy coefficient $K_g = 9.36 \times 10^{-22}$ J is selected from the considerations to have the magnetic length in units of lattice constants a equal $\ell = a\sqrt{|J_g/K_g|} = 5a$ reasonable for numeric calculations. For a semiclassical model (C1), the spin length scales the total energy. In our simulations, the spin length is set to be $S = 1/2$. The Gilbert damping $\alpha_G = 1$ is chosen from the considerations of the speeding up the relaxation dynamics. In the following, J_b^{ij} and K_b are used for the intergrain exchange coupling and anisotropy for the spins at the grain boundaries, respectively, $j = \langle J_b^{ik} \rangle / J_g$ is the dimensionless average intergrain exchange. The zero-field cooling process in simulations is emulated by the relaxation dynamics started from the random initial state with the relaxation time $t_{fin} = 16$ ns to obtain the final equilibrium state for further analysis. Equation (C2) is integrated using the midpoint scheme with 0.01 ps time steps. In simulations with the predefined domain wall and uniform patterns, the magnetic moments were randomly tilted up to 0.05 radians from the easy axis. For a square lattice with magnetic moments $\mathbf{m}_i$ labeled as $\mathbf{A}_\nu$, $\mathbf{B}_\nu$, $\mathbf{C}_\nu$, $\mathbf{D}_\nu$ within the νth antiferromagnetic unit cell in the counterclockwise order, $\mathbf{n}_\nu = \mathbf{A}_\nu - \mathbf{B}_\nu + \mathbf{C}_\nu - \mathbf{D}_\nu$ [45,77], see Figs. 1(d) and 1(e). The index ν is omitted for simplicity.

Spin lattice simulations and training of the neural network was done at the high-performance computing cluster of the Helmholtz-Zentrum Dresden-Rossendorf [70].

APPENDIX D: MACHINE LEARNING

The residual neural network (ResNet18) [47] has been trained by means of the Python software tool PyTorch [78]. The relevant feature of this neural network is the presence of additional connections between neighbor layers of weights, which solves the problem of a small gradient for the first neural layers and accelerates the training of weights, see Fig. S6 within the Supplemental Material [38]. The neural-network topology ResNet18 [47] was used due to the insignificant size of the dataset. The dataset consists of binarized images of antiferromagnetic domain patterns obtained from simulations and from scanning N-V magnetomertry, which are rescaled to the size of 224×224 pixels, and contains 16 convolutional layers.

To train the neural network, we use 27 different pairs (j, σ) (see set of parameters in Fig. S7 within the Supplemental Material [38] and training error in Fig. S8 within the Supplemental Material [38]). For each of these sets of parameters, 50 simulations were performed to generate the dataset. The trained network is used for classifying domain patterns whose binarized versions are shown in insets of Fig. S9 within the Supplemental Material [38]. This gives an estimation of the intergrain exchange as $j = 0.11 \pm 0.02$ and $\sigma = 0.16 \pm 0.01$, where the accuracy limit is related to the neural-network output.

APPENDIX E: CHARACTERIZATION OF DOMAINS PATTERNS MEASURED USING SCANNING N-*V* MAGNETOMETRY

We characterize domain patterns by calculating their fractal dimension. A bulklike domain wall is almost straight or weakly curved [27] and is characterized by $d_{c1} = 1$. The limiting case of a space-filling curve, which fully covers the plane, corresponds to $d_{c2} = 2$.

To calculate d_c, we binarize the experimentally taken N-*V* images and apply the procedure (1), see Fig. S9 within the Supplemental Material [38]. At small spatial scales, the slope gradually decreases because of better matching the square pixel structure of images with the covering squares of ϵ side size. The fractal dimension for the scales supporting self-similarity reads

$$d_c = 1.76 \pm 0.06. \tag{E1}$$

APPENDIX F: MODEL OF INHOMOGENEOUS EXCHANGE

Within the model, which is referred to as the model of inhomogeneous exchange, the exchange bonds are classified as follows: there are (i) antiferromagnetic intragrain bonds with the exchange integral $J^{ik} = J_g$ [orange lines in Figs. 1(d), 5(b) and 5(c) and red line in Fig. S10(a) within the Supplemental Material [38]] and (ii) intergrain bonds with $J^{ik} = J_b$ ($|J_b| < |J_g|$) for all respective i, j [black lines in Fig. 1(d)]. The grain boundary is determined by the cross section of the corresponding exchange bond by the edge of the Voronoi pattern. Within the framework of the inhomogeneous exchange model, the intergrain exchange J_b is taken to be the same for all boundary sites, i.e., $\sigma = 0$. The fractal dimension remains constant at $d_c \approx 1$ for $0.25 \lesssim j \leq 1$, see the red line in Fig. S10(b) within the Supplemental Material [38]. Within the range $|j| \leq 0.25$, the fractal dimension quickly grows to the maximal value $d_c^{\max} \approx 1.98$. We note that the bulklike domain walls are captured in simulations only due to finite time of observation, which does not allow the domain walls to be eliminated in full as a consequence of the slow relaxation dynamics.

An example of the evolution of a domain pattern is shown in Fig. 2. The interval of values of the intergrain exchange, resulting in simulated domain patterns characterized by a similar fractal dimension as the experimentally observed pattern, is $0.07 \lesssim J_b/J_g \lesssim 0.094$.

APPENDIX G: MODEL OF RANDOM EXCHANGE

Within the model referred to as the model of random exchange, we analyze domain patterns in the case of randomly distributed values of exchange integrals at grain boundaries (distribution of the exchange bond values is different in comparison with the model of the inhomogeneous exchange). Several examples of the distributions are shown in Figs. S10(a) and S11(a) within the Supplemental Material [38]. The variation of the mean value of the intergrain exchange $j = \langle J_b/J_g \rangle$ and the corresponding standard deviation σ allows to include both ferromagnetic and antiferromagnetic bonds between grains and in this way to control the rate of frustration in the system. Figure S12 within the Supplemental Material [38] shows schematics of the spin lattice with a grain boundary and the distribution of exchange bond parameters in simulations. We illustrate this model for the simplest case when the grain boundary is aligned with the crystallographic axis. In this case, each boundary spin has three strong antiferromagnetic bonds belonging to the grain. The fourth bond can be weaker antiferromagnetic (depicted as orange) or ferromagnetic (depicted as green). The corresponding type of the exchange bond (either ferro- or antiferromagnetic) is shown by black lines in Fig. 1(d). Domain patterns for the large standard deviation is shown in Fig. S13 within the Supplemental Material [38].

A sufficiently narrow Gaussian distribution for exchange bonds leads to the behavior quantitatively similar to the case simulated within the model of the inhomogeneous exchange, see red and black symbols in Fig. S10(b) within the Supplemental Material [38]. For larger σ, the curve $d_c(j)$ shifts towards larger fractal dimensions for the same j and the horizontal space it occupies shrinks.

Figures S3–S5 within the Supplemental Material [38] represent a detailed analysis of the distribution of small domains for the selected states shown in Figs. 4(g)–4(i). We compute the distribution of small domains in simulations by sampling historgrams up to $6S_0$ (Fig. S3 within the Supplemental Material [38]), $8S_0$ (Fig. S4 within the Supplemental Material [38], corresponds to the experiment), and $15S_0$ (Fig. S5 within the Supplemental Material [38]), where S_0 is the average grain area. The distributions, which are similar to the bimodal distribution observed for the experimental data [Fig. 4(b)], are highlighted by green background. According to the fractal dimensions [Fig. S10(b) within the Supplemental Material [38]], the relevant exchange parameters at grain boundary are as

follows: $0.07 \lesssim j \lesssim 0.094$ for $\sigma = 0$, $0.09 \lesssim j \lesssim 0.13$ for $\sigma = 0.2 J_g$ and $0.127 \lesssim j \lesssim 0.19$ for $\sigma = 0.4 J_g$.

Figure S14 within the Supplemental Material [38] shows the bit error rate for writing "1" bit sequences (red) into the initial "0" state (blue). In comparison with Fig. 7, here, the same relative scale of the grain lateral size and magnetic length is used as estimated for the experimental samples (Figs. 1–5). Smaller average grain size leads to the need to use more grains per domain to achieve low bit error rates. This is due to larger curvature of domain walls bounding domains with a semicircular shape.

In Fig. S15 within the Supplemental Material [38], initial and final states for the different distances between bits are shown. If the distance between bits is too close (less than the lateral size of three average grains), there is a high probability that two neighboring bits will form one domain instead of several domains, which are separated by the initial (blue) state. This happens because a sufficiently large grain with strong coupling with its neighbors can appear between neighboring bits, which makes their position loosely defined. The number of grains per bit for different writing success values is shown in Fig. S16 within the Supplemental Material [38].

Here, we calculate the potential capacity of one inch² as follows. For $l_g = 50$ nm and 10 grains per bit, the bit lateral size is 158 nm. Together with surrounding of 6ℓ with $\ell = 20$ nm for the Cr_2O_3. The total area occupied by one bit is about $(398 \text{ nm})^2 \approx 158.5 \times 10^3 \text{ nm}^2$, which gives 3.79 Gbit/inch². To estimate the lateral grain size to achieve 1 Tbit/inch², ten grains per bit and four grains for the bit surrounding are used with the same procedure.

APPENDIX H: MODEL OF INHOMOGENEOUS ANISOTROPY

Within the model referred to as the model of inhomogeneous anisotropy, it is possible to take into account that the broken lattice structure at grain boundaries can lead to the change of the spin-orbit interaction and the corresponding reduction of the uniaxial anisotropy. We vary the anisotropy coefficient for all boundary sites [see sites with black bonds in Fig. 1(d)] in the range $K^i = K_b \in [-K_g, K_g]$. The uniform ordering of the Néel vector along the anisotropy axis is stable within the entire range of anisotropy values at grain boundaries. For a weak easy-axis anisotropy, domain walls exhibit a weak pinning at inhomogeneities of the material parameters and reveal a tendency to be expelled from the sample during the relaxation process with $d_c = 1$, see Fig. S10(c) within the Supplemental Material [38] (red open symbols). The relaxation rate $\max_i |d\mathbf{m}_i/dt|$ at $t = t_{\text{fin}}$ is typically at least one order of magnitude higher than for the models of inhomogeneous and random exchange considered above. This is an indication that the domain pattern is not stable, see Fig. S2 within the Supplemental Material [38]. This behavior of

domain patterns is similar to the one observed for domain walls in single crystals.

APPENDIX I: MODEL OF RANDOM ANISOTROPY

In the same way as for the model of random exchange, we vary the anisotropy at grain boundaries using a truncated normal distribution. The results are similar to those obtained within the model of inhomogeneous anisotropy, see Figs. S10(c) and S18(f)–(g) within the Supplemental Material [38].

APPENDIX J: COMPARISON OF MODELS OF A GRANULAR THIN-FILM ANTIFERROMAGNET

Models with the constant and random intergrain coupling considered above show qualitatively the same and quantitatively close domain patterns, although there is a strong difference between changing the exchange bonds and changing of anisotropy at grain boundaries. We note that the pinning strength of domain walls in the models of inhomogeneous and random exchange is much stronger than in the models of inhomogeneous and random anisotropy. This is reflected in the relaxation dynamics, see Fig. S2 within the Supplemental Material [38]. The thermalization in simulations involving the variation of J^{ik} reveals intermittent flips of single spins at final stages. In contrast, in the case of varying K^i, even at final stages of the relaxation process, we observe jumps of domain walls between neighboring grain boundaries.

Comparing the fractal dimensions estimated within different models described above, we conclude that the variation of the anisotropy at grain boundaries itself cannot be the decisive factor responsible for the pinning of domain walls.

APPENDIX K: REGULAR GRAIN PATTERNS

To check the influence of the random grain shape and their random spatial distribution, we perform simulations with two types of regular grain patterns, i.e., square and hexagonal patterns. The obtained results are qualitatively and quantitatively coincide with the case of random grains, c.f. Figs. S17 and S10 within the Supplemental Material [38]. We note, that the square grain pattern tends to form the antiferromagnetic superlattice for low values of j.

[1] Y. Cao, G. Xing, H. Lin, N. Zhang, H. Zheng, and K. Wang, Prospect of spin-orbitronic devices and their applications, iScience **23**, 101614 (2020).

[2] X. Han, X. Wang, C. Wan, G. Yu, and X. Lv, Spin-orbit torques: Materials, physics, and devices, Appl. Phys. Lett. **118**, 120502 (2021).

[3] H. Yang, S. O. Valenzuela, M. Chshiev, S. Couet, B. Dieny, B. Dlubak, A. Fert, K. Garello, M. Jamet, D.-E. Jeong, K. Lee, T. Lee, M.-B. Martin, G. S. Kar, P. Sénéor, H.-J. Shin, and S. Roche, Two-dimensional materials prospects for non-volatile spintronic memories, Nature **606**, 663 (2022).

[4] A. Hoffmann and W. Zhang, Antiferromagnets for spintronics, J. Magn. Magn. Mater. **553**, 169216 (2022).

[5] A. Qaiumzadeh, I. A. Ado, R. A. Duine, M. Titov, and A. Brataas, Theory of the Interfacial Dzyaloshinskii-Moriya Interaction in Rashba Antiferromagnets, Phys. Rev. Lett. **120**, 197202 (2018).

[6] R. M. Otxoa, P. E. Roy, R. Rama-Eiroa, J. Godinho, K. Y. Guslienko, and J. Wunderlich, Walker-like domain wall breakdown in layered antiferromagnets driven by staggered spin–orbit fields, Commun. Phys. **3**, 190 (2020).

[7] F. Xue and P. M. Haney, Intrinsic staggered spin-orbit torque for the electrical control of antiferromagnets: Application to CrI_3, Phys. Rev. B **104**, 224414 (2021).

[8] S. Ghosh, A. Manchon, and J. Železný, Unconventional Robust Spin-Transfer Torque in Noncollinear Antiferromagnetic Junctions, Phys. Rev. Lett. **128**, 097702 (2022).

[9] L. Šmejkal, Y. Mokrousov, B. Yan, and A. H. MacDonald, Topological antiferromagnetic spintronics, Nat. Phys. **14**, 242 (2018).

[10] O. Gomonay, V. Baltz, A. Brataas, and Y. Tserkovnyak, Antiferromagnetic spin textures and dynamics, Nat. Phys. **14**, 213 (2018).

[11] X. He, W. Echtenkamp, and C. Binek, Scaling of the magnetoelectric effect in chromia thin films, Ferroelectrics **426**, 81 (2012).

[12] S. P. Pati, M. Al-Mahdawi, S. Ye, Y. Shiokawa, T. Nozaki, and M. Sahashi, Finite-size scaling effect on néel temperature of antiferromagnetic $Cr_2O_3(0001)$ films in exchange-coupled heterostructures, Phys. Rev. B **94**, 224417 (2016).

[13] Y. Kota and H. Imamura, Narrowing of antiferromagnetic domain wall in corundum-type Cr_2O_3 by lattice strain, Appl. Phys. Exp. **10**, 013002 (2017).

[14] A. Mahmood, W. Echtenkamp, M. Street, J.-L. Wang, S. Cao, T. Komesu, P. A. Dowben, P. Buragohain, H. Lu, A. Gruverman, A. Parthasarathy, S. Rakheja, and C. Binek, Voltage controlled Néel vector rotation in zero magnetic field, Nat. Commun. **12**, 1674 (2021).

[15] P. Makushko, *et al.*, Flexomagnetism and vertically graded Néel temperature of antiferromagnetic Cr_2O_3 thin films, Nat. Commun. **13**, 6745 (2022).

[16] V. M. Kalita, A. F. Lozenko, S. M. Ryabchenko, and P. A. Trotsenko, The role of defects in the formation of the multidomain state of easy-plane antiferromagnets with magnetoelastic interaction, J. Exp. Theor. Phys. **99**, 1054 (2004).

[17] E. G. Galkina, V. E. Kireev, R. V. Ovcharov, R. S. Khymyn, and B. A. Ivanov, Spin dynamics in antiferromagnets with domain walls and disclinations, Ukrainian J. Phys. **65**, 924 (2020).

[18] K. Y. Jing, C. Wang, and X. R. Wang, Random walk of antiferromagnetic skyrmions in granular films, Phys. Rev. B **103**, 174430 (2021).

[19] P. Wadley, *et al.*, Electrical switching of an antiferromagnet, Science **351**, 587 (2016).

[20] T. Janda, *et al.*, Magneto-Seebeck microscopy of domain switching in collinear antiferromagnet CuMnAs, Phys. Rev. Mater. **4**, 094413 (2020).

[21] S. Y. Bodnar, L. Šmejkal, I. Turek, T. Jungwirth, O. Gomonay, J. Sinova, A. A. Sapozhnik, H.-J. Elmers, M. Kläui, and M. Jourdan, Writing and reading antiferromagnetic Mn_2Au by Néel spin-orbit torques and large anisotropic magnetoresistance, Nat. Commun. **9**, 348 (2018).

[22] M. Bibes and A. Barthélémy, Towards a magnetoelectric memory, Nat. Mater. **7**, 425 (2008).

[23] S. Manipatruni, D. E. Nikonov, C.-C. Lin, T. A. Gosavi, H. Liu, B. Prasad, Y.-L. Huang, E. Bonturim, R. Ramesh, and I. A. Young, Scalable energy-efficient magnetoelectric spin–orbit logic, Nature **565**, 35 (2018).

[24] N. A. Spaldin and R. Ramesh, Advances in magnetoelectric multiferroics, Nat. Mater. **18**, 203 (2019).

[25] X. He, Y. Wang, N. Wu, A. N. Caruso, E. Vescovo, K. D. Belashchenko, P. A. Dowben, and C. Binek, Robust isothermal electric control of exchange bias at room temperature, Nat. Mater. **9**, 579 (2010).

[26] T. Kosub, M. Kopte, R. Hühne, P. Appel, B. Shields, P. Maletinsky, R. Hübner, M. O. Liedke, J. Fassbender, O. G. Schmidt, and D. Makarov, Purely antiferromagnetic magnetoelectric random access memory, Nat. Commun. **8**, 13985 (2017).

[27] N. Hedrich, K. Wagner, O. V. Pylypovskyi, B. J. Shields, T. Kosub, D. D. Sheka, D. Makarov, and P. Maletinsky, Nanoscale mechanics of antiferromagnetic domain walls, Nat. Phys. **17**, 574 (2021).

[28] P. Appel, B. J. Shields, T. Kosub, N. Hedrich, R. Hübner, J. Faßbender, D. Makarov, and P. Maletinsky, Nanomagnetism of magnetoelectric granular thin-film antiferromagnets, Nano Lett. **19**, 1682 (2019).

[29] S. Ye, Y. Shiokawa, S. P. Pati, and M. Sahashi, Parasitic magnetism in magnetoelectric antiferromagnet, ACS Appl. Mater. Interfaces **12**, 29971 (2020).

[30] I. Veremchuk, M. O. Liedke, P. Makushko, T. Kosub, N. Hedrich, O. V. Pylypovskyi, F. Ganss, M. Butterling, R. Hübner, E. Hirschmann, A. G. Attallah, A. Wagner, K. Wagner, B. Shields, P. Maletinsky, J. Fassbender, and D. Makarov, Defect nanostructure and its impact on magnetism of α-Cr_2O_3 thin films, Small **18**, 2201228 (2022).

[31] A. Erickson, S. Q. Abbas Shah, A. Mahmood, I. Fescenko, R. Timalsina, C. Binek, and A. Laraoui, Nanoscale imaging of antiferromagnetic domains in epitaxial films of Cr_2O_3 via scanning diamond magnetic probe microscopy, RSC Adv. **13**, 178 (2023).

[32] E. V. Gomonay and V. M. Loktev, On the theory of the formation of equilibrium domain structure in antiferromagnets, Low Temp. Phys. **30**, 804 (2004).

[33] H. V. Gomonay and V. M. Loktev, Shape-induced phenomena in finite-size antiferromagnets, Phys. Rev. B **75**, 174439 (2007).

[34] I. Veremchuk, P. Makushko, N. Hedrich, Y. Zabila, T. Kosub, M. O. Liedke, M. Butterling, A. G. Attallah, A. Wagner, U. Burkhardt, O. V. Pylypovskyi, R. Hübner, J. Fassbender, P. Maletinsky, and D. Makarov, Magnetism and magnetoelectricity of textured polycrystalline bulk Cr_2O_3 sintered in conditions far out of equilibrium, ACS Appl. Electron. Mater. **4**, 2943 (2022).

[35] U. Kwon, R. Sinclair, E. Velu, S. Malhotra, and G. Bertero, Ru/Ru-oxide interlayers for CoCrPtO perpendicular recording media, IEEE Trans. Magn. **41,** 3193 (2005).

[36] A. Q. Wu, E. K. C. Chang, Y. Zhao, H. Zhou, K. Gao, J.-U. Thiele, M. Seigler, G. Ju, E. Gage, Y. Kubota, T. Klemmer, T. Rausch, C. Peng, Y. Peng, D. Karns, X. Zhu, and Y. Ding, HAMR areal density demonstration of 1+ Tbpsi on spinstand, IEEE Trans. Magn. **49,** 779 (2013).

[37] T. R. Albrecht, *et al.*, Bit-patterned magnetic recording: Theory, media fabrication, and recording performance, IEEE Trans. Magn. **51,** 1 (2015).

[38] See Supplemental Material at http://link.aps.org/supplemental/10.1103/PhysRevApplied.20.014020 for additional figures.

[39] I. E. Dzialoshinskii, Thermodynamic theory of "weak" ferromagnetism in antiferromagnetic substances, Sov. Phys. JETP **5,** 1259 (1957).

[40] A. Parthasarathy and S. Rakheja, Dynamics of Magnetoelectric Reversal of an Antiferromagnetic Domain, Phys. Rev. Appl. **11,** 034051 (2019).

[41] K. D. Belashchenko, Equilibrium Magnetization at the Boundary of a Magnetoelectric Antiferromagnet, Phys. Rev. Lett. **105,** 147204 (2010).

[42] I. Thomas and J. Wikswo, Reconstruction of two-dimensional magnetization and susceptibility distributions from the magnetic field of soft magnetic materials, IEEE Trans. Magn. **32,** 230 (1996).

[43] E. A. Lima and B. P. Weiss, Obtaining vector magnetic field maps from single-component measurements of geological samples, J. Geophys. Res. **114,** B06102 (2009).

[44] F. Casola, T. van der Sar, and A. Yacoby, Probing condensed matter physics with magnetometry based on nitrogen-vacancy centres in diamond, Nat. Rev. Mater. **3,** 17088 (2018).

[45] S. Komineas and N. Papanicolaou, Traveling skyrmions in chiral antiferromagnets, SciPost Phys. **8,** 86 (2020).

[46] P. Virtanen, *et al.*, SciPy 1.0: Fundamental algorithms for scientific computing in Python, Nat. Methods **17,** 261 (2020).

[47] K. He, X. Zhang, S. Ren, and J. Sun, in *2016 IEEE Conference on Computer Vision and Pattern Recognition (CVPR)* (IEEE, 2016).

[48] D.-H. Kim, Y.-C. Cho, S.-B. Choe, and S.-C. Shin, Correlation between fractal dimension and reversal behavior of magnetic domain in Co/Pd nanomultilayers, Appl. Phys. Lett. **82,** 3698 (2003).

[49] F. C. Moon, *Chaotic Vibrations* (Wiley-VCH, Hoboken, New Jersey, 2004), 309.

[50] F. V. Lisovskii, L. I. Lukashenko, and E. G. Mansvetova, Thermodynamically stable fractal-like domain structures in magnetic films, J. Exp. Theor. Phys. Lett. **79,** 352 (2004).

[51] G. Catalan, H. Béa, S. Fusil, M. Bibes, P. Paruch, A. Barthélémy, and J. F. Scott, Fractal Dimension and Size Scaling of Domains in Thin Films of Multiferroic BiFeO₃, Phys. Rev. Lett. **100,** 027602 (2008).

[52] J. Li, J. Pelliciari, C. Mazzoli, S. Catalano, F. Simmons, J. T. Sadowski, A. Levitan, M. Gibert, E. Carlson, J.-M. Triscone, S. Wilkins, and R. Comin, Scale-invariant magnetic textures in the strongly correlated oxide NdNiO₃, Nat. Commun. **10,** 4568 (2019).

[53] K. E. Siewierska, N. Teichert, R. Schafer, and J. M. D. Coey, Imaging domains in a zero-moment half metal, IEEE Trans. Magn. **55,** 1 (2019).

[54] C. G. Granqvist and R. A. Buhrman, Ultrafine metal particles, J. Appl. Phys. **47,** 2200 (1976).

[55] A. S. Kovalev and A. M. Kosevich, Dislocations and domains in antiferromagnets (short note), Low Temp. Phys. (Fiz. Nizk. Temp.) **3,** 259 (1977).

[56] I. E. Dzyaloshinskiĭ, Domains and dislocations in antferromagnets, Pis'ma Zh. Exp. Teor. Fiz. **25,** 110 (1977).

[57] O. K. Dudko and A. S. Kovalev, Influence of dislocations on the magnetic structure of two-dimensional anisotropic antiferromagnets, Low Temp. Phys. **26,** 603 (2000).

[58] V. E. Kireev and B. A. Ivanov, Localized magnetic non-uniformities in an antiferromagnet with a system of dislocations, Low Temp. Phys. **45,** 1256 (2019).

[59] S. Reimers, D. Kriegner, O. Gomonay, D. Carbone, F. Krizek, V. Novák, R. P. Campion, F. Maccherozzi, A. Björling, O. J. Amin, L. X. Barton, S. F. Poole, K. A. Omari, J. Michalička, O. Man, J. Sinova, T. Jungwirth, P. Wadley, S. S. Dhesi, and K. W. Edmonds, Defect-driven antiferromagnetic domain walls in CuMnAs films, Nat. Commun. **13,** 724 (2022).

[60] N. Wu, X. He, A. L. Wysocki, U. Lanke, T. Komesu, K. D. Belashchenko, C. Binek, and P. A. Dowben, Imaging and Control of Surface Magnetization Domains in a Magnetoelectric Antiferromagnet, Phys. Rev. Lett. **106,** 087202 (2011).

[61] S. Cao, M. Street, J. Wang, J. Wang, X. Zhang, C. Binek, and P. A. Dowben, Magnetization at the interface of Cr₂O₃ and paramagnets with large stoner susceptibility, J. Phys.: Condens. Matter **29,** 10LT01 (2017).

[62] M. Grzybowski, P. Wadley, K. Edmonds, R. Beardsley, V. Hills, R. Campion, B. Gallagher, J. Chauhan, V. Novak, T. Jungwirth, F. Maccherozzi, and S. Dhesi, Imaging Current-Induced Switching of Antiferromagnetic Domains in CuMnAs, Phys. Rev. Lett. **118,** 057701 (2017).

[63] S.-W. Cheong, M. Fiebig, W. Wu, L. Chapon, and V. Kiryukhin, Seeing is believing: visualization of antiferromagnetic domains, npj Quantum Mater. **5,** 3 (2020).

[64] P. Schoenherr, L. Giraldo, M. Lilienblum, M. Trassin, D. Meier, and M. Fiebig, Magnetoelectric force microscopy on antiferromagnetic 180° domains in Cr₂O₃, Materials **10,** 1051 (2017).

[65] T. Ashida, M. Oida, N. Shimomura, T. Nozaki, T. Shibata, and M. Sahashi, Isothermal electric switching of magnetization in Cr₂O₃/Co thin film system, Appl. Phys. Lett. **106,** 132407 (2015).

[66] F. Matsukura, Y. Tokura, and H. Ohno, Control of magnetism by electric fields, Nat. Nanotechnol. **10,** 209 (2015).

[67] Y. Wang, H. Fang, C. L. Zacherl, Z. Mei, S. Shang, L.-Q. Chen, P. D. Jablonski, and Z.-K. Liu, First-principles lattice dynamics, thermodynamics, and elasticity of Cr₂O₃, Surf. Sci. **606,** 1422 (2012).

[68] M. Fechner, A. Sukhov, L. Chotorlishvili, C. Kenel, J. Berakdar, and N. A. Spaldin, Magnetophononics: Ultrafast spin control through the lattice, Phys. Rev. Mater. **2,** 064401 (2018).

[69] J. Li, C. B. Wilson, R. Cheng, M. Lohmann, M. Kavand, W. Yuan, M. Aldosary, N. Agladze, P. Wei, M. S. Sherwin,

and J. Shi, Spin current from sub-terahertz-generated anti-ferromagnetic magnons, Nature **578**, 70 (2020).

[70] High performance computing at Helmholtz–Zentrum Dresden–Rossendorf, http://www.hzdr.de.

[71] L. Rondin, J.-P. Tetienne, T. Hingant, J.-F. Roch, P. Maletinsky, and V. Jacques, Magnetometry with nitrogen-vacancy defects in diamond, Rep. Prog. Phys. (2014),.

[72] N. Hedrich, D. Rohner, M. Batzer, P. Maletinsky, and B. J. Shields, Parabolic Diamond Scanning Probes for Single-Spin Magnetic Field Imaging, Phys. Rev. Appl. **14**, 064007 (2020).

[73] R. S. Schoenfeld and W. Harneit, Real Time Magnetic Field Sensing and Imaging using a Single Spin in Diamond, Phys. Rev. Lett. **106**, 030802 (2011).

[74] S. Jenkins, A. Meo, L. E. Elliott, S. K. Piotrowski, M. Bapna, R. W. Chantrell, S. A. Majetich, and R. F. L. Evans, Magnetic stray fields in nanoscale magnetic tunnel junctions, J. Phys. D: Appl. Phys. **53**, 044001 (2020).

[75] SLaSi spin–lattice simulations package.

[76] S. Shi, A. L. Wysocki, and K. D. Belashchenko, Magnetism of chromia from first-principles calculations, Phys. Rev. B **79**, 104404 (2009).

[77] S. Komineas and N. Papanicolaou, Vortex dynamics in two-dimensional antiferromagnets, Nonlinearity **11**, 265 (1998).

[78] A. Paszke, *et al.*, in *Advances in Neural Information Processing Systems 32* (Curran Associates, Inc., 2019), p. 8024.